JOURNAL OF GEOPHYSICAL RESEARCH, VOL. 114, D08103, doi:10.1029/2008JD010616, 2009

Improvements in land surface temperature retrieval from the Landsat series thermal band using water vapor and air temperature

J. Cristóbal,[1] J. C. Jiménez-Muñoz,[2] J. A. Sobrino,[2] M. Ninyerola,[3] and X. Pons[1,4]

Received 16 June 2008; revised 14 November 2008; accepted 26 January 2009; published 16 April 2009.

[1] Land surface temperature (LST) is involved in many land surface processes such as evapotranspiration, net radiation, or air temperature modeling. In this paper we present an improved methodology to retrieve LST from Landsat 4 TM, Landsat 5 TM, and Landsat 7 ETM+ using four atmospheric databases covering different water vapor ranges (from 0 to 8 g cm^{-2}) to build the LST retrieval models and using both water vapor and air temperature as input variables. We also compare this with LST retrievals using only water vapor or only air temperature, as well as with an existing LST retrieval algorithm. In order to validate the results, we have selected 77 Landsat images taken between 2002 and 2006 (Catalonia, northeast of the Iberian Peninsula) and two sources of water vapor (radiosounding data and remote sensing estimations) and air temperature (radiosounding data and air temperature modeling). The best results using radiosounding data are obtained when both air temperature and water vapor are present in the LST retrieval models with a mean RMSE of 0.9 K, followed by only water vapor models with a mean RMSE of 1.5 K and only air temperature models with a mean RMSE of 5.6 K. The results obtained using Terra Moderate Resolution Imaging Spectroradiometer (MODIS) Level 2 water vapor product and at-satellite-pass air temperature modeling as input data also show that this kind of input data offers best results, with a mean RMSE of 0.9 K, followed by water vapor models with a mean RMSE of 2.1 K and only air temperature models with a mean RMSE of 5.6 K. Similar errors when using radiosounding or modeled water vapor and air temperature as input data suggest the avoidance of radiosounding data to retrieve LST over extensive areas. Finally, when comparing the presented methodology with another methodology also using water vapor and air temperature as input data, the improvement is of more than 0.5 K.

Citation: Cristóbal, J., J. C. Jiménez-Muñoz, J. A. Sobrino, M. Ninyerola, and X. Pons (2009), Improvements in land surface temperature retrieval from the Landsat series thermal band using water vapor and air temperature, *J. Geophys. Res.*, *114*, D08103, doi:10.1029/2008JD010616.

1. Introduction

[2] Land surface temperature (LST) is one of the most important sources of input data in land surface processes such as actual and potential evapotranspiration or net radiation [*Bastiaanssen et al.*, 1998; *Cristóbal et al.*, 2005; *Dash et al.*, 2002; *Hurtado and Sobrino*, 2001; *Jackson et al.*, 1981; *Kustas*, 1996; *Kustas et al.*, 2003; *Quattrochi and Luvall*, 2000] and is involved in many important ecological processes. Furthermore, LST is also used in the development of several indexes such as Stress Degree Day or Crop Water Stress Index, which are used to evaluate stress over crops areas [*Jackson et al.*, 1977; *Moran et al.*, 1994] as well as in air temperature modeling [*Cristóbal et al.*, 2008; *Riddering and Queen*, 2006].

[3] Nowadays, it is clear that thermal sensors aboard satellite platforms used to monitor land surface processes over ecosystems at a global and regional scale are the only feasible way to obtain LST measurements owing to their high sampling rate and repetitive basis over large and heterogeneous regions. There are several platforms that currently include in its sensor configuration one or more thermal bands such as NOAA AVHRR, Terra/Aqua MODIS, Terra ASTER, Meteosat or Envisat ATSR in their sensor configuration. Most of them have been developed to monitor meteorological parameters and are designed with a coarse spatial resolution, often greater than 1000 m at nadir, but with a good temporal resolution, for instance a twice-a-day revisit period. Although these satellites offer a wide swath that makes it possible to cover a very large area, part of the image (beyond 25° off-nadir) displays a bow-tie

[1]Department of Geography, Autonomous University of Barcelona, Cerdanyola del Vallès, Spain.
[2]Global Change Unit, Imaging Processing Laboratory, Department of Earth Physics and Thermodynamics, University of Valencia, Paterna, Spain.
[3]Unit of Botany, Department of Animal Biology, Plant Biology and Ecology, Autonomous University of Barcelona, Cerdanyola del Vallès, Spain.
[4]Center for Ecological Research and Forestry Applications, Autonomous University of Barcelona, Cerdanyola del Vallès, Spain.

0148-0227/09/2008JD010616$09.00

effect being extreme pixels of low utility because of their deformation [*Yang and Di*, 2004].

[4] Depending on the region where land surface processes are monitored, higher spatial resolution is needed. An example is the Mediterranean region, a heterogeneous region with a high level of habitat fragmentation due to human activity, climate and relief. If a better spatial resolution and continuous and global coverage are needed, only Landsat missions can offer these possibilities because, currently, Terra-ASTER does not offer them owing to its image acquisition policy. Furthermore, there is also an uncertainty related to the inclusion of a thermal band on board the future NASA Landsat Data Continuity Mission (LDCM), which could jeopardize well-developed water irrigation plans [*Anderson and Kustas*, 2008] and many other studies related with land surface processes. We hope that future missions give an adequate continuity to the Landsat thermal band legacy.

[5] Currently, there are only two satellite programs that have given us more than 25 years of thermal information of great value: TIROS/NOAA and Landsat, although only Landsat program have taken thermal images at medium spatial resolution. Landsat 4 TM, that was launched in 1982 and terminated its service in 1993, was the first sensor of the series that present a thermal band in its configuration. Landsat 5 TM, which was launched in 1984, and Landsat 7 ETM+, that was launched in 1999, continued including a thermal band and are still operative, although experiencing a number of problems, especially in the case of Landsat 7 ETM+. Landsat thermal data have been used in numerous studies such as thermal plume analysis [*Gibbons et al.*, 1989; *Shanmugam et al.*, 2006], volcano activity monitoring [*Kaneko and Wooster*, 1999], coal fire detection [*Mansor and Cracknell*, 1994; *Saraf et al.*, 1995; *Zhang and van Genderen*, 1997], evapotranspiration retrieval and water irrigation planning and monitoring [*Allen et al.*, 2007; *Bastiaanssen et al.*, 1998; *Kustas et al.*, 2004; *Yang et al.*, 1997], air temperature modeling [*Cristóbal et al.*, 2008], urban heat analysis [*Xian and Crane*, 2006; *Stathopoulou and Cartalis*, 2007], crop water stress index development [*Moran et al.*, 1989, 1994], among others.

[6] However, one of the main limitations of Landsat thermal information is the presence of only one band in the thermal spectral region. This makes it more difficult to perform atmospheric correction compared with other satellites, like NOAA-AVHRR or Terra-ASTER, which have two or more thermal bands. There have been several attempts to correct the Landsat thermal band atmospherically [*Bartolucci and Chang*, 1988; *Gibbons et al.*, 1989; *Mansor and Cracknell*, 1994; *Goetz et al.*, 1995; *Schneider and Mauser*, 1996; *Hurtado et al.*, 1996]. Most of these methodologies require information from atmospheric radiosoundings to perform atmospheric correction. However, it should be taken into account that a single atmospheric radiosounding is not representative of the entire Landsat image atmospheric conditions (about 180 by 185 km), especially in areas with highly variable relief. In order to retrieve LST, but avoiding dependence on radiosounding data as well as obtaining LST over extensive areas, *Qin et al.* [2001] and *Jiménez-Muñoz and Sobrino* [2003] developed a methodology based on the radiative transfer equation using the Landsat 5 TM thermal band. *Qin et al.* [2001] developed a monowindow algorithm using water vapor and air temperature as input data for the model in which two atmospheric parameters are required for the algorithm: transmittance and effective mean atmospheric temperature. Method about determination of atmospheric transmittance is given through the simulation of atmospheric conditions with LOWTRAN 7 program. In the case of the estimation of the effective mean atmospheric temperature a practicable approach from local meteorological observation was also proposed when the in situ atmospheric profile data is unavailable at the satellite pass. However, one of the main limitations of this model is the range of water vapor for which it was designed, 0 to 3 g cm^{-2}, which limits LST retrieval beyond these values. Moreover, there is no reference to the source to be used to obtain air temperature, an important practical issue when one wishes to retrieve LST over large areas. The *Jiménez-Muñoz and Sobrino* [2003] model is only water-vapor-dependent, which minimizes the input data required and then provides an operational methodology to retrieve LST from the Landsat 5 thermal band. Since input data were minimized to only one atmospheric parameter, an error in the water vapor source could increase the error in LST retrieval, and also errors in LST are higher when increasing the atmospheric water vapor content. In fact, for water vapor contents higher than 3 g cm^{-2}, the single-channel algorithm is not accurate enough and it should not be applied. This is due to the uncertainties introduced when fitting atmospheric parameters only to the water vapor, which are dramatically propagated to the LST retrievals. This problem is common to any technique based on a direct single-channel inversion of the radiative transfer equation, in which the final retrievals are very sensitive to uncertainties on the input parameters. The Jiménez-Muñoz and Sobrino model has been updated and extended to Landsat 4 and Landsat 7 thermal bands in work by *Jiménez-Muñoz et al.* [2009]. In that work, the authors also analyze the feasibility of using Look-Up Tables (LUTs) to avoid the problem related to the uncertainties introduced in the fitting between atmospheric parameters and water vapor.

[7] This problem can be also solved by incorporating to the model the air temperature, at the expense of requiring two atmospheric parameters as input data. In order to analyze the importance of air temperature in LST retrieval, this article aims to do the following.

[8] 1. We will improve LST retrievals by introducing also the air temperature in the single-channel algorithm presented by *Jiménez-Muñoz and Sobrino* [2003] and *Jiménez-Muñoz et al.* [2009].

[9] 2. We will test the models obtained using a set of 77 Landsat images (58 Landsat 5 TM and 19 Landsat 7 ETM+) taken between 2002 and 2006 and compare the results with *Qin et al.* [2001] LST retrieval methodology (only in the case of Landsat 5 TM). In addition, we will use as input data water vapor and air temperature obtained from radiosoundings and Terra MODIS water vapor product and an existing air temperature regionalization methodology [*Cristóbal et al.*, 2008].

2. Land Surface Temperature Algorithm Development

[10] This section is divided into four subsections. In the first subsection we describe the LST retrieval algorithms. In

the second subsection we fit and test the atmospheric functions. Moreover, we present the final parameters to compute the atmospheric functions for each Landsat satellite. In the third subsection we present a sensitivity analysis of the variables involved in the model. In the fourth subsection we present a description of the atmospheric databases used to compute the model.

2.1. Algorithm Theoretical Basis

[11] The most suitable procedure to retrieve LST from a single-channel located in the thermal infrared region, as is the case of the Landsat thermal band, is by the inversion of the radiative transfer equation (RTE) based on the following expression applied to a certain sensor channel (or wavelength interval):

$$L_{sensor,\lambda} = \left[\varepsilon_\lambda B_\lambda(T_s) + (1-\varepsilon_\lambda)L^{\downarrow}_{atm,\lambda}\right]\tau_\lambda + L^{\uparrow}_{atm,\lambda}, \quad (1)$$

where L_{sensor} is at-sensor radiance, ε is the surface emissivity, λ is the wavelength, T_s is the land surface temperature (LST), $L_{\text{atm},\lambda}\downarrow$ is the downwelling atmospheric radiance (hemispherical flux divided by pi), $L_{\text{atm},\lambda}\uparrow$ is the upwelling atmospheric radiance (path radiance at λ wavelength) and τ is the atmospheric transmissivity. Radiances are in W m^{-2} sr^{-1} μm^{-1} and wavelength in μm. B term is Planck's law, expressed as follows:

$$B_\lambda(T_s) = \frac{c_1}{\lambda^5\left[\exp\left(\frac{c_2}{\lambda T_s}\right)-1\right]}, \quad (2)$$

where c_1 and c_2 are Planck's radiation constants, with values of 1.19104×10^8 W μm^4 m^{-2} sr^{-1} and 1.43877×10^4 μm K, respectively. Note that the above mentioned spectral magnitudes should be integrated over a band pass (filter response function) in the case of Landsat.

[12] In the work of *Jiménez-Muñoz and Sobrino* [2003] a single-channel method based on the radiative transfer equation was developed and, according to these authors, LST can be retrieved using this equation:

$$\text{LST} = \gamma\left[\varepsilon^{-1}(\psi_1 L_{\text{sensor}} + \psi_2) + \psi_3\right] + \delta, \quad (3)$$

where

$$\gamma = \left\{\frac{c_2 L_{sensor}}{T^2_{sensor}}\left[\frac{\lambda^4_{eff}}{c_1}L_{sensor} + \lambda^{-1}_{eff}\right]\right\}^{-1} \quad (4)$$

$$\delta = -\gamma L_{sensor} + T_{sensor}, \quad (5)$$

where T_{sensor} is the apparent brightness temperature in K, calculated according to equation (13), and ψ_1, ψ_2, ψ_3 are the atmospheric functions (ψ_1 is dimensionless and ψ_2 and ψ_3 have units of radiance, W m^{-2} sr^{-1} μm). The λ_{eff} is the effective wavelength and is defined as

$$\lambda_{\text{eff}} = \frac{\int \lambda f_\lambda d\lambda}{\int f_\lambda d\lambda}, \quad (6)$$

where f_λ is obtained from the spectral responsivity of the band of the Landsat thermal given by *Irish* [2003]. Once λ_{eff} is computed, its value is 11.154 for Landsat 4 TM, 11.457 for Landsat 5 TM and 11.270 for Landsat 7 ETM+.

[13] In the work of *Jiménez-Muñoz and Sobrino* [2003] the atmospheric functions ψ_1, ψ_2, ψ_3 (henceforth referred to as AF1, AF2 and AF3, respectively) are obtained as a function of the total atmospheric water vapor content (w), owing to the fact that this component is the main absorber in the thermal infrared region. However, in this work we have also introduced air temperature (T_a) to compute the atmospheric functions (AFs) because of its close relationship with the atmospheric parameters used to retrieve LST. Another attempt to introduce air temperature together with w are given by *Qin et al.* [2001], who developed a mono-window algorithm to retrieve LST.

2.2. Building New Atmospheric Functions: Statistical Fit and Test

[14] As we have described in the previous section, in order to retrieve LST, *Jiménez-Muñoz and Sobrino* [2003] developed atmospheric functions which were only dependent on w. However, in this work these functions will also be dependent on both w and T_a or only on T_a. Therefore, three sets of atmospheric functions will be defined for each Landsat sensor using these equations:

$$\text{AF}_{1(w,T_a)} \equiv \frac{1}{\tau_{(w,T_a)}}, \quad (7)$$

$$\text{AF}_{2(w,T_a)} \equiv -L^{\downarrow}_{atm(w,T_a)} - \frac{L^{\uparrow}_{atm(w,T_a)}}{\tau_{(w,T_a)}}, \quad (8)$$

$$\text{AF}_{3(w,T_a)} \equiv L^{\downarrow}_{atm(w,T_a)}, \quad (9)$$

where w is the water vapor in g cm^{-2} and T_a is the near surface air temperature in K. Although these functions are also wavelength-dependent, in order to obtain a better interpretation of the atmospheric functions this parameter has not been included. Furthermore, in the case of Landsat satellites, the thermal band is always designed with the same wavelength width, from 10.5 to 12.5 μm.

[15] Before statistically fit the AFs, we need a source of atmospheric parameters ($L\uparrow$, $L\downarrow$ and τ) to compute them. These atmospheric parameters have been extracted from four world-wide-scale atmospheric radiosounding databases which cover different water vapor ranges (see section 2.4). Therefore, we have obtained different sets of AFs depending on the Landsat satellite mission and depending on the atmospheric database used. Atmospheric parameters ($L\downarrow$, $L\uparrow$, τ) have been obtained by a simulation procedure using the MODTRAN 4.0 radiative transfer code [*Kneisys et al.*, 1995] and weighted depending on the thermal band filter function configuration.. To predict the atmospheric parameters, MODTRAN 4.0 code has been executed in thermal radiance with multiple scattering mode for a view angle of nadir and for clear-sky conditions (see Figure 1).

[16] Once the atmospheric functions have been computed we have statistically fitted these values with a second degree

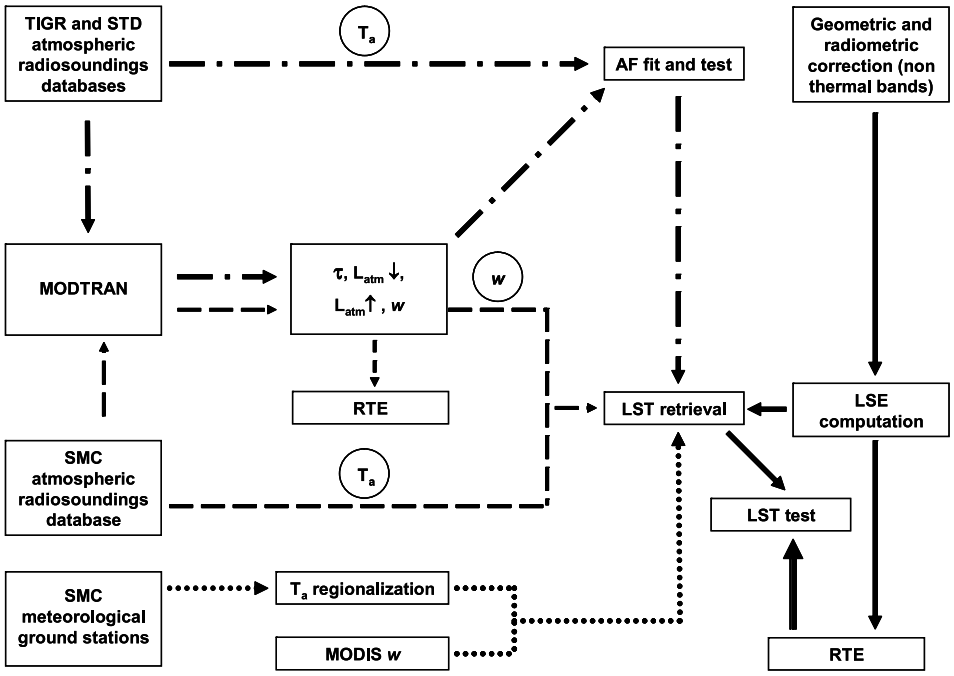

Figure 1. Flow chart for LST retrieval and test methodologies. RTE is the radiative transfer equation (equation (1)), SMC is the Catalan Meteorological Service, T_a is the air temperature, w is the water vapor, LSE is the land surface emissivity, AF are the atmospheric functions, LST is the land surface temperature, τ is the transmissivity, L_{atm}, $\downarrow$ is the downwelling atmospheric radiance, and L_{atm} $\uparrow$ is the upwelling atmospheric radiance.

polynomial based on w (equation (10)), on w and T_a (equation (11)) and on T_a (equation (12)),

$$AF_n = iw^2 + hT_a^2 + gw + fT_a + eT_a^2w + dT_aw + cT_aw^2 + bT_a^2w^2 + a, \quad (10)$$

$$AF_n = iw^2 + gw + a, \quad (11)$$

$$AF_n = hT_a^2 + fT_a + a, \quad (12)$$

where n = 1, 2, 3 and subscripts a, b, c, d, e, f, g, h and i are the numerical coefficients of the statistical fit. T_a used to adjust the AFs has been extracted from the first level of the atmospheric radiosoundings, taking this temperature to be near-surface temperature, and w was modeled using MODTRAN 4.0. Tables 1 and 2 show the numerical coefficients of the AFs using w and T_a and only T_a for each atmospheric database used and for the different Landsat missions. The coefficients of the AFs using only w is given by *Jiménez-Muñoz et al.* [2009].

[17] In order to apply a test to the atmospheric functions we have selected two sets of radiosoundings for each atmospheric database by means of a stratified random sampling according to the type of radiosounding (tropical, midlatitude summer, midlatitude winter and subarctic summer or subarctic winter). We have selected 60% of the radio soundings to fit the model and the remaining 40% to perform the test. However, it is important to note that the numerical coefficients in Tables 1 and 2 have been computed using all atmospheric radiosoundings.

[18] Tables 3 and 4 show the total number of radio soundings used to fit and test the models depending on the atmospheric database and the coefficients of determination of the test over the models. In the case of AFs developed using only w results is given by *Jiménez-Muñoz et al.* [2009]. In the case of AFs modeled using only w or w and T_a, the test coefficients of determination (R^2) range from 0.95 to nearly 1.00. In the case of AFs modeled using only T_a, worse results have been obtained. This can be explained by the fact that although air temperature correlates well with $L\downarrow$ and $L\uparrow$ (mainly, AF2 and AF3), this is not enough to obtain an optimal model.

2.3. Sensitivity Analysis

[19] In order to analyze the impact of the error on LST retrieval, we have performed a sensitivity analysis over w and T_a. A typical RMSE obtained in T_a modeling is about 1.7 K [*Cristóbal et al.*, 2008] and in the case of w is about 0.5 g cm^{-2} [*Sobrino and El Kharraz*, 2003] (also B.-C. Gao and Y. J. Kaufman, MODIS Near-IR water vapor algorithm: Total precipitable water, algorithm technical background document, 1998, http://modis.gsfc.nasa.gov/data/atbd/atmos_atbd.php) (hereinafter, Gao and Kaufman, online document, 1998). We have carried out this analysis for each one of the radiosoundings of the four atmospheric databases used (TIGR-1, TIGR-2, TIGR-3 and STD) and for the models developed using T_a (LSTT), w (LSTw) and both w and T_a (LSTwT) for Landsat 4 TM, Landsat 5 TM and Landsat 7 ETM+. When this analysis is performed, we

Table 1. Numerical Coefficients for AFs Modeled With w and T_a Depending on the Atmospheric Database Used and the Landsat Mission[a]

	Mission	AF	i	h	g	f	e	d	c	b	a
TIGR-1	L4	AF1	2.3133	0.0001	−11.6383	−0.0460	−0.0002	0.0871	−0.01728	0.0001	7.0747
		AF2	−25.6858	0.0003	170.3620	−0.1125	0.0020	−1.1829	0.18810	−0.0003	10.8481
		AF3	9.4518	−0.0008	−64.3221	0.4001	−0.0006	0.4079	−0.06238	0.0001	−49.4918
	L5	AF1	1.6374	0.0002	−22.1873	−0.1203	−0.0003	0.1668	−0.01457	0.0001	16.9590
		AF2	−20.8105	−0.0007	254.5604	0.3888	0.0032	−1.8110	0.16857	−0.0003	−56.0719
		AF3	8.7659	−0.0008	−74.9773	0.4164	−0.0007	0.4803	−0.05805	0.0001	−51.5311
	L7	AF1	2.4096	0.0001	−12.1968	−0.0489	−0.0002	0.0914	−0.01803	0.0001	7.4514
		AF2	−25.8763	0.0002	174.2737	−0.0753	0.0021	−1.2139	0.19022	−0.0003	6.1264
		AF3	9.0725	−0.0007	−63.9035	0.3754	−0.0006	0.4073	−0.06007	0.0001	−46.4043
TIGR-2	L4	AF1	−2.1465	0.0001	−9.3417	−0.0382	−0.0001	0.0733	0.01216	−0.0001	5.9215
		AF2	14.7239	−0.0002	85.1399	0.1180	0.0011	−0.6252	−0.08040	0.0001	−16.4527
		AF3	−3.1879	−0.0002	−21.7049	0.0949	−0.0002	0.1364	0.02166	−0.0001	−11.1518
	L5	AF1	−2.1465	0.0001	−9.3417	−0.0382	−0.0001	0.0733	0.01216	−0.0001	5.9215
		AF2	14.7239	−0.0002	85.1399	0.1180	0.0011	−0.6252	−0.08040	0.0001	−16.4527
		AF3	−3.1879	−0.0002	−21.7049	0.0949	−0.0002	0.1364	0.02166	−0.0001	−11.1518
	L7	AF1	−1.9215	0.0001	−8.0103	−0.0291	−0.0001	0.0626	0.01102	−0.0001	4.7624
		AF2	13.9594	−0.0001	72.9618	0.0557	0.0009	−0.5299	−0.07831	0.0001	−8.4889
		AF3	−3.3697	−0.0002	−19.3512	0.0973	−0.0002	0.1194	0.02306	−0.0001	−11.4877
TIGR-3	L4	AF1	−0.3520	0.0001	−7.2789	−0.0394	−0.0001	0.0565	0.00119	0.0000	5.9913
		AF2	−14.7195	−0.0001	94.2853	0.0306	0.0011	−0.6614	0.10819	−0.0002	−5.1866
		AF3	7.4846	−0.0003	−32.3407	0.1650	−0.0003	0.2024	−0.04930	0.0001	−19.8025
	L5	AF1	−0.5106	0.0001	−8.6391	−0.0571	−0.0001	0.0680	0.00190	0.0000	8.2010
		AF2	−15.2043	−0.0003	107.0078	0.1627	0.0013	−0.7646	0.11442	−0.0002	−21.7580
		AF3	7.5944	−0.0003	−33.7379	0.1419	−0.0003	0.2146	−0.05035	0.0001	−16.9315
	L7	AF1	−0.6714	0.0001	−6.3120	−0.0293	−0.0001	0.0490	0.00346	0.0000	4.6656
		AF2	−9.7513	0.0002	79.3508	−0.0871	0.0009	−0.5488	0.07298	−0.0001	10.2461
		AF3	6.9548	−0.0003	−30.3594	0.1708	−0.0003	0.1887	−0.04567	0.0001	−20.6465
STD	L4	AF1	−2.0551	0.0002	−12.1648	−0.1166	−0.0002	0.0964	0.01157	−0.0000	16.3935
		AF2	76.8511	−0.0001	−21.7522	0.0687	−0.0001	0.1081	−0.50670	0.0008	−7.5969
		AF3	−29.9226	−0.0011	71.5054	0.5973	0.0010	−0.5380	0.21132	−0.0004	−79.4362
	L5	AF1	−10.7274	0.0003	−11.8802	−0.1711	−0.0002	0.1010	0.06910	−0.0001	23.6178
		AF2	142.9898	−0.0008	−25.3735	0.4416	−0.0001	0.0862	−0.94533	0.0015	−57.1427
		AF3	−37.7736	−0.0011	69.2553	0.5709	0.0001	−0.5170	0.26283	−0.0005	−75.7081
	L7	AF1	−2.2457	0.0002	−12.6518	−0.1224	−0.0002	0.1004	0.01273	−0.0000	17.1599
		AF2	78.1645	−0.0002	−18.4200	0.1185	−0.0001	0.0802	−0.51446	0.0008	−14.0342
		AF3	−28.6515	−0.0011	67.9536	0.5663	0.0010	−0.5113	0.20226	−0.0004	−75.3498

[a]Numerical coefficients are a, b, c, d, e, f, g, h, and i. Missions: L4, Landsat 4 TM; L5, Landsat 5 TM; L7, Landsat 7 ETM+. TIGR and STD are the atmospheric databases.

see that, regarding w, 68% of the cases of computing LST has an error lower than 1 K while, regarding T_a, 57% of the cases of computing LST has an error lower than 1 K, suggesting that an improvement in T_a estimation is an important topic of future research.

[20] Emissivity and effective wavelength error analysis have been developed by *Jiménez-Muñoz and Sobrino* [2003, 2006] and, according to these authors, an error in emissivity of 1% leads to an error of 0.6 K in LST retrieval, while, in the case of effective wavelength, an error of 3% results in an error of 0.5 K in LST retrieval.

2.4. Description of the Atmospheric Radio Soundings Database

[21] Four atmospheric databases have been used to compute the atmospheric functions. The first three databases are the three versions of the Thermodynamic Initial Guess Retrieval data tank [*Scott and Chedin*, 1981; *Chédin et al.*, 1985; *Achard*, 1991; *Chevallier et al.*, 1998; *Aires et al.*, 2002] called TIGR-1, TIGR-2 and TIGR-3, respectively.

[22] The TIGR-1 is composed of 861 atmospheres. However, we have used a selection of 61 atmospheres from TIGR1 (28 atmospheres assigned to the tropical model, 12 to the midlatitude summer model, 12 to the subarctic winter and 9 to the U.S. Standard) created by *Sobrino et al.* [1993], which have been used in several studies, including the development of the *Jiménez-Muñoz and Sobrino* [2003] model. Figure 2 shows the total water vapor content for all atmospheres and ranges from 0.21 to 5.97 g cm^{-2} with a mean of 2.94 g cm^{-2} and a σ of 1.75 g cm^{-2}.

[23] The TIGR-2 data set is a revision of TIGR1 and is composed of 1761 atmospheres (assigned to the following model atmospheres: 322 tropical, 388 midlatitude summer, 354 midlatitude winter, 104 subarctic summer and 593 subarctic winter). Figure 2 shows the total water vapor content for all atmospheres and ranges from 0.05 to 7.68 g cm^{-2} with a mean of 1.04 g cm^{-2} and a σ of 1.14 g cm^{-2}.

[24] The TIGR-3 data set includes 2311 atmospheres on a world-wide scale and is useful for computing global atmospheric functions (assigned to the following model atmospheres: 872 tropical, 388 midlatitude summer, 354 midlatitude winter, 104 subarctic summer and 593 subarctic winter). Figure 2 shows the total water vapor content for all atmospheres, which range from 0.05 to 8.31 g cm^{-2} with a mean of 1.83 g cm^{-2} and a σ of 1.83 g cm^{-2}. Figure 3 shows the spatial distribution of the TIGR-3 atmosphere database.

Table 2. Numerical Coefficients for AFs Modeled for Only T_a Depending on the Atmospheric Database Used and the Landsat Mission[a]

	Model	AF	*h*	*f*	*a*
TIGR-1	L4	AF1	0.0008	−0.4265	56.3130
		AF2	−0.0096	4.9770	−642.6641
		AF3	0.0023	−1.1818	148.2818
	L5	AF1	0.0009	−0.4854	64.0614
		AF2	−0.0104	5.3685	−693.9884
		AF3	0.0023	−1.1465	143.3814
	L7	AF1	0.0009	−0.4482	59.1220
		AF2	−0.0098	5.0746	−655.0991
		AF3	0.0023	−1.1335	141.8605
TIGR-2	L4	AF1	0.0005	−0.2670	35.0801
		AF2	−0.0062	3.1456	−400.2054
		AF3	0.0018	−0.9188	114.9932
	L5	AF1	0.0005	−0.2731	35.8816
		AF2	−0.0063	3.2355	−411.9907
		AF3	0.0019	−0.9615	120.6194
	L7	AF1	0.0005	−0.2455	32.3409
		AF2	−0.0059	3.0203	−384.5072
		AF3	0.0019	−0.9490	119.1746
TIGR-3	L4	AF1	0.0006	−0.3085	40.1687
		AF2	−0.0073	3.6996	−468.4755
		AF3	0.0020	−1.0028	124.4097
	L5	AF1	0.0007	−0.3644	47.2779
		AF2	−0.0080	4.0796	−516.6649
		AF3	0.0020	−0.9769	120.7640
	L7	AF1	0.0006	−0.3270	42.4381
		AF2	−0.0075	3.7864	−478.3716
		AF3	0.0019	−0.9265	113.9363
STD	L4	AF1	0.0014	−0.7798	106.0954
		AF2	−0.0168	9.0498	−1216.3357
		AF3	0.0045	−2.3952	318.4317
	L5	AF1	0.0016	−0.8452	114.9039
		AF2	−0.0176	9.4979	−1276.5364
		AF3	0.0045	−2.3776	315.8949
	L7	AF1	0.0015	−0.8187	111.3313
		AF2	−0.0171	9.2303	−1240.4405
		AF3	0.0044	−2.3174	307.8070

[a]Numerical coefficients are *a*, *f*, and *h*. Missions: L4, Landsat 4 TM; L5, Landsat 5 TM; L7, Landsat 7 ETM+. TIGR and STD are the atmospheric databases.

[25] Finally, we have constructed an additional database by considering the 6 standard atmospheric profiles (tropical, midlatitude summer, midlatitude winter, subarctic summer, subarctic winter and U. S. Standard) included in the MODTRAN code and a scaling water vapor factor from 0.5 to 1.5 in steps of 0.1. This leads to a total of 66 atmospheres; we have labeled this database STD. Figure 2 shows the total water vapor content for all atmospheres and ranges from 0.21 to 6.17 g cm^{-2} with a mean of 1.97 g cm^{-2} and a σ of 1.47 g cm^{-2}.

[26] Each atmosphere includes altitude, pressure, temperature and humidity profiles from which we have computed the τ, the w, the $L\downarrow$ and the $L\uparrow$ used in the atmospheric functions computation using MODTRAN 4.0. The remaining atmospheric constituents were assigned to the appropriate standard atmosphere included in the MODTRAN 4.0 code.

3. Model Test With Independent Data: Test Areas and Data Processing

[27] This section is divided into two subsections. In the first subsection we present the study area where the validation process was developed. The second subsection describes the meteorological and remote sensing data processing. Figure 1 shows a flow chart of the LST retrieval and test methodologies.

Table 3. Determination Coefficients of the Atmospheric Function Tests for Models That Include Water Vapor and Air Temperature, Depending on the Atmospheric Database Used

		R^2 Test (40%)				
	Database	AF1	AF2	AF3	n Fit[a]	n Test[a]
Landsat 4	STD	0.99	0.99	0.99	40	26
	TIGR-1	0.98	0.98	0.97	37	24
	TIGR-2	0.98	0.98	0.99	1073	688
	TIGR-3	0.96	0.96	0.99	1370	941
Landsat 5	STD	0.99	0.99	0.99	40	26
	TIGR-1	0.98	0.98	0.97	37	24
	TIGR-2	0.98	0.98	0.99	1073	688
	TIGR-3	0.96	0.96	0.99	1370	941
Landsat 7	STD	0.99	0.99	0.99	40	26
	TIGR-1	0.98	0.98	0.97	37	24
	TIGR-2	0.98	0.98	0.99	1073	688
	TIGR-3	0.96	0.96	0.99	1370	941

[a]Here n denotes number of samples used.

3.1. Test Areas

[28] The geographical boundary of the study area is located in Catalonia (in the northeast of the Iberian Peninsula) and is defined by the following UTM-31 N coordinates (in km): 260 (minimum X), 528 (maximum X), 4489 (minimum Y) and 4749 (maximum Y) with a total area of approximately 32000 km^2 (see Figure 4).

[29] In order to validate the methodology we have selected two sets (Barcelona and Sort) of test sites within a 20 km buffer area from where the atmospheric radio soundings are launched (see section 3.2). These test sites for each set include vegetation with high coverage (>80%), medium coverage (between 50 and 80%), low coverage (between 20 and 50%) and bare soils (<20%). Vegetation coverage has been computed using equation (17) and a land cover map (J. J. Ibàñez and J. A. Burriel, MCSC: A high-resolution thematic digital cartography, paper presented at the 5th European Congress on Regional Geoscientific Cartography and Information Systems, Institut Cartogràfic de Catalunya, Barcelona, Spain, 2006) and a vegetation map (Generalitat de Catalunya, Cartografia dels hàbitats a Cata-

Table 4. Determination Coefficients of the Atmospheric Function Tests for Models That Only Include Air Temperature, Depending on the Atmospheric Database Used

		R^2 Test (40%)				
	Database	AF1	AF2	AF3	n Fit[a]	n Test[a]
Landsat 4	STD	0.56	0.63	0.72	40	26
	TIGR-1	0.26	0.32	0.40	37	24
	TIGR-2	0.45	0.56	0.77	1073	688
	TIGR-3	0.54	0.63	0.80	1370	941
Landsat 5	STD	0.56	0.63	0.71	40	26
	TIGR-1	0.26	0.31	0.40	37	24
	TIGR-2	0.45	0.56	0.77	1073	688
	TIGR-3	0.53	0.62	0.80	1370	941
Landsat 7	STD	0.56	0.63	0.72	40	26
	TIGR-1	0.26	0.32	0.40	37	24
	TIGR-2	0.46	0.57	0.76	1073	688
	TIGR-3	0.54	0.64	0.80	1370	941

[a]Here n denotes number of samples used.

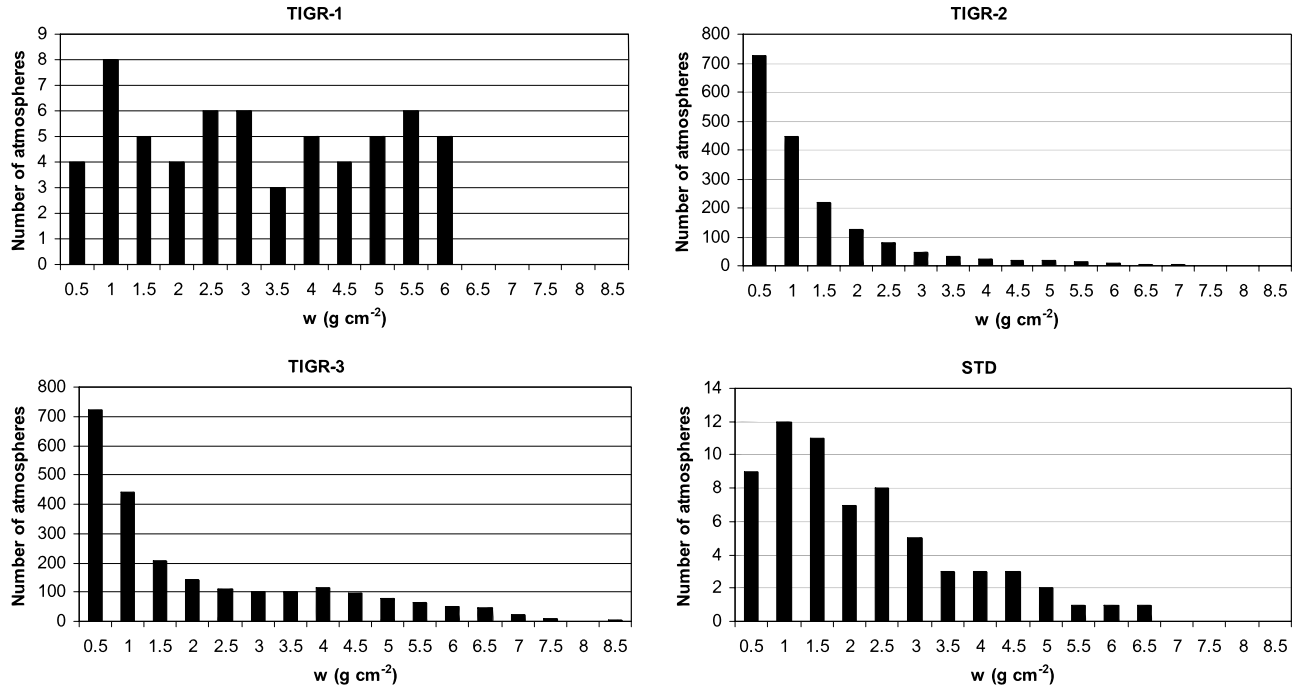

Figure 2. Water vapor content of the TIGR-1, TIGR-2, TIGR-3, and STD atmospheric databases.

lunya, 1:50.00, per fulls de tall 1:50.000, 2007, http://mediambient.gencat.net/cat/el_departament/cartografia/fitxes/habitats.jsp?ComponentID = 5523&SourcePageID = 6463#1).

[30] As mentioned in section 2.3, an error of 1% in emissivity results in an error of 0.6 K in LST retrieval. Owing to the absence of ε direct measurements, we have tried to select validation areas with low σ_ε (standard deviation of ε). Table 5 shows the ε and the $\sigma\varepsilon$ for all validation areas. In addition, we have chosen areas which are at least 3 by 3 thermal band pixels.

[31] In the case of the Barcelona radiosounding area (BCN), we have selected 3 test sites of high coverage (numbers 1, 2 and 3 in Figure 4), 2 test sites of medium

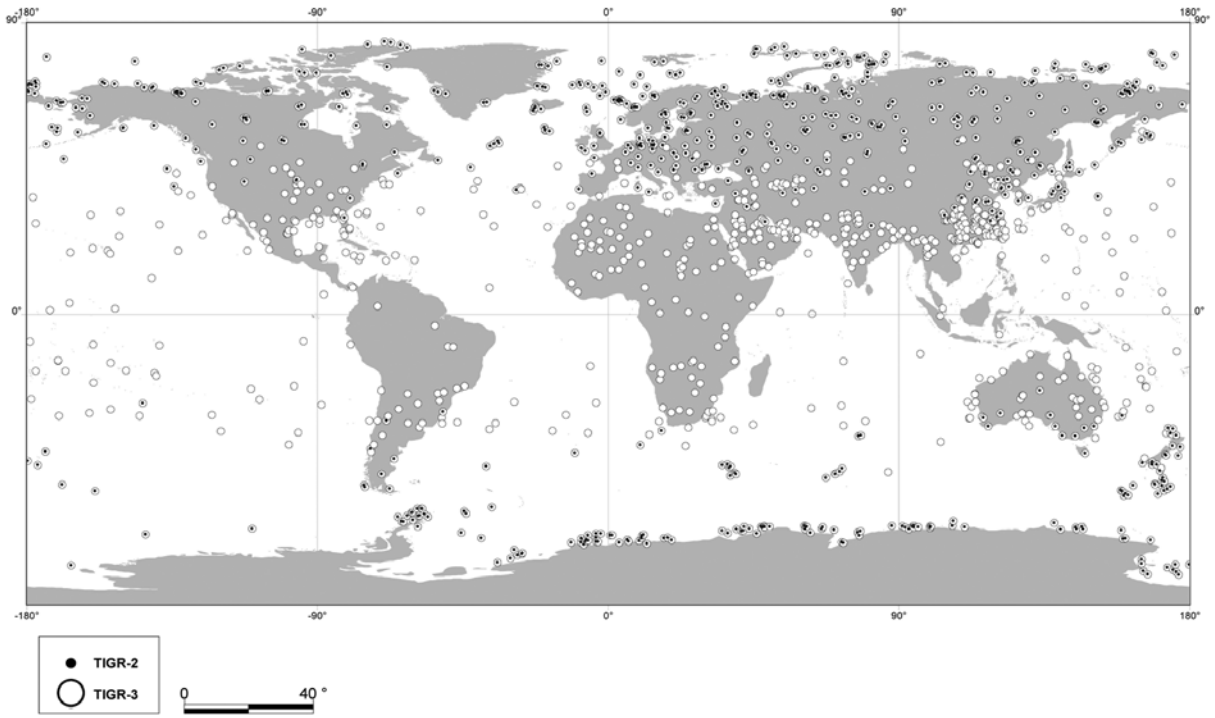

Figure 3. Spatial distribution of the TIGR-2 and TIGR-3 databases.

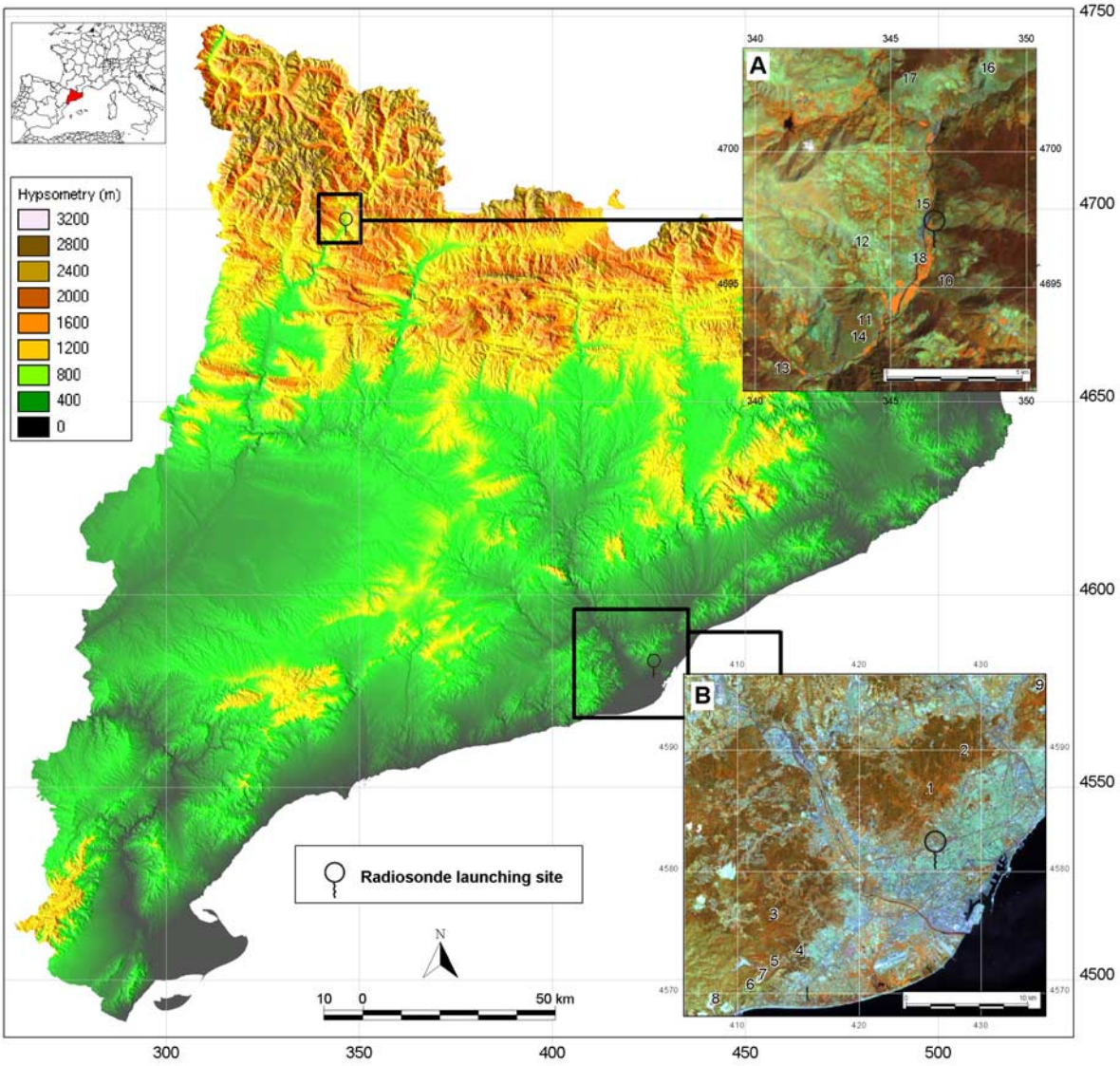

Figure 4. General view of Catalonia and the validation sites, in Universal Transversal Mercator (UTM) projection (UTM coordinates are expressed in kilometers). Numbers from 1 to 18 are the validation sites. Image A is the SORT study area (background image is a 4 + 5 + 3 composite from a Landsat 5 TM of 18 August 2003) and image B is the BCN study area (background image is a 4 + 5 + 3 composite from a Landsat 7 ETM+ of 13 June 2002).

coverage (numbers 4 and 5), 1 test site of low coverage (number 6) and 3 sites of bare soils (numbers 7, 8 and 9). In the case of the Sort radiosounding area (SORT), we have selected 3 test sites of high coverage (numbers 10, 11 and 12), 3 test sites of medium coverage (numbers 13, 14 and 15) and 3 sites of low coverage (numbers 16, 17 and 17).

3.2. Meteorological and Remote Sensing Data Processing

[32] We have processed 154 meteorological ground stations and an atmospheric radiosounding database (see Figure 4) from the Catalan Meteorological Service, SMC, (data available at http://www.meteocat.com). These radio soundings are launched at 0000 and at 1200 UTC and include altitude, pressure, air temperature and humidity profiles. BCN radiosounding point, at 72 m a.s.l., presents a mean w of 1.79 and a σ of 0.81 g cm^{-2} with a minimum of 0.16 and a maximum of 5.00 g cm^{-2}. SORT radiosounding point is launched in the pre-Pyrenees at 680 m a.s.l. and presents a mean w of 1.01 and a σ of 0.54 g cm^{-2} with a minimum of 0.25 and a maximum of 2.37 g cm^{-2}.

[33] A set of 77 Landsat images (58 Landsat 5 TM and 19 Landsat 7 ETM+ from path/row 197/031 and 198/031–032) from 2002 and 2006 were selected to carry out the model validation. Dates were selected with the aim of covering all months of the year to take into account different daily situations.

[34] Finally, Terra MODIS Level 2 water vapor images (MOD05_L2) were downloaded from the Level 1 and

Table 5. Emissivity and Its Standard Deviation at the Validation Sites[a]

Category	Mean ε	$\sigma\varepsilon$	n
	BCN		
Veg (h Pv) 1	0.986	0.006	61
Veg (h Pv) 2	0.984	0.005	44
Veg (h Pv) 3	0.985	0.004	61
Veg (m Pv) 1	0.979	0.008	61
Veg (m Pv) 2	0.979	0.006	62
Veg (l Pv) 1	0.972	0.007	61
Soil 1	0.963	0.008	62
Soil 2	0.967	0.006	61
Soil 3	0.970	0.004	61
	SORT		
Veg (h Pv) 1	0.991	0.007	4
Veg (h Pv) 2	0.987	0.004	4
Veg (h Pv) 3	0.985	0.000	4
Veg (m Pv) 1	0.985	0.000	4
Veg (m Pv) 2	0.985	0.000	4
Veg (m Pv) 3	0.987	0.008	4
Veg (l Pv) 1	0.968	0.007	4
Veg (l Pv) 2	0.978	0.009	4
Veg (l Pv) 3	0.971	0.007	4

[a]Emissivity, ε; its standard deviation, σ_ε; h Pv indicates a high proportion of vegetation, m Pv is a medium proportion of vegetation, and l Pv indicates a low proportion of vegetation. Veg is natural vegetation, soil is bare soil, and n is the number of samples.

Atmosphere Archive and Distribution System (data available at http://ladsweb.nascom.nasa.gov/).

[35] The computation of Landsat 5 TM and Landsat 7 ETM+ images was carried out using the following methodologies.

3.2.1. Geometric Correction

[36] Images have been corrected using conventional techniques based on first-order polynomials taking into account the effect of the relief of the land surface using a Digital Elevation Model [*Palà and Pons*, 1995] obtaining a RMSE of less than 30 m even in the most extreme altitudes. The spatial resolution of all Landsat 7 ETM+ and Landsat 5 TM bands has been resampled to Landsat 5 TM thermal band spatial resolution, 120 m.

3.2.2. Radiometric Correction (Nonthermal Bands)

[37] Radiometric correction to obtain at-surface reflectances has been carried out using the methodology proposed by *Pons and Solé-Sugrañes* [1994]. This allows us to reduce the number of undesired artifacts that are due to the effects of the atmosphere or to differential illumination which is, in turn, due to the time of day, location on the Earth and relief (some zones are more illuminated than others, cast shadows, etc.). Conversion from digital numbers to TOA radiances has been carried out using image header parameters taking into account the comments of *Cristóbal et al.* [2004].

3.2.3. Apparent Brightness Temperature

[38] Apparent brightness temperature or at-sensor brightness temperature, T_{sensor}, is usually computed by means of Planck's law inversion and in the case of Landsat series, *Schott and Volchok* [1985], *Markham and Barker* [1986] and *Irish* [2003] proposed a simplified methodology,

$$T_{sensor} = \frac{K2}{\ln(K1/L_\lambda + 1)}, \tag{13}$$

where K1 (W m^{-2} sr^{-1} μm^{-1}) and K2 (K) are calibration constants based on the Landsat thermal band configuration and L_λ is the spectral radiance (W m^{-2} sr^{-1} μm^{-1}). In the case of Landsat 4 TM, K1 and K2 are 671.62 and 1284.3, respectively. In the case of Landsat 5 TM, K1 and K2 are 607.76 and 1260.6, respectively. Finally, in the case of Landsat 7 ETM+ K1 and K2 are 666.09 and 1282.7, respectively.

[39] L_λ is calculated using the conversion parameters from DN to radiance included in the original image metadata using this equation:

$$L_\lambda = a\ DN + b, \tag{14}$$

where $L_{sensor\lambda}$ is the at-sensor radiance, DN is the digital number and a and b are the conversion coefficients. Table 6 shows these coefficients in the case of TM and ETM+ sensors [*Barsi et al.*, 2003, 2007; *Schott et al.*, 2001]. It is important to note that if these conversion coefficients are not available in the image metadata, certain facts should be taken into account [*Cristóbal et al.*, 2004].

3.2.3.1. Image Processing Format

[40] Images delivered by USGS (NLAPS format) or by ESA (LPGS format) are processed differently. NLAPS format considers the 0 value as NODATA as well as a radiometric value. LPGS format considers the 0 value only as NODATA and the radiances are rescaled from 1 to 255 DN. Table 6 shows the different values of a and

Table 6. Conversion Parameters From DN to Radiances of Landsat Sensors Depending on the Image Processing Date and the Processing Format[a]

Sensor	Parameter	Mode	Image Acquisition	Image Processing Date	NASA NLAPS Format	ESA LPGS Format	Min Rad	Max Rad
ETM+	a	Low gain		Before 1 July 2002	0.066823	0.067087	0.00	17.04
	b	Low gain		Before 1 July 2002	0.000000	−0.067087	0.00	17.04
ETM+	a	High gain		After 1 July 2002	0.037059	0.037205	3.20	12.65
	b	High gain		After 1 July 2002	3.200000	3.16279	3.20	12.65
TM	a		From 1 March 1984 to 4 May 2003		0.055158	0.055512	1.24	15.25
	b		From 1 March 1984 to 4 May 2003		1.237800	1.144488	1.24	15.25
TM	a		After 4 May 2003		0.055158	0.055512	1.20	15.30
	b		After 4 May 2003		1.237800	1.144489	1.20	15.30

[a]Rad, radiance; min, minimum; max, maximum; ESA, European Space Agency; NASA, National Aeronautics and Space Administration; NLAPS, National Landsat Archive Processing System; LPGS, Level 1 Product Generation Systems. Radiance units in W m^{-2} sr^{-1} μm^{-1}.

b (see columns 6 and 7, respectively) depending on the processing image format.

3.2.3.2. Image Processing Date

[41] This case only occurs in the ETM+ sensor and depending on the processing date, different a and b coefficients should be applied (see column 5 of Table 6).

3.2.4. Land Surface Emissivity (LSE)

[42] There are several methodologies to compute LSE [*Rubio et al.*, 1997; *Sobrino and Raissouni*, 2000; *Valor and Caselles*, 2005; *Sobrino et al.*, 2008]. To compute LSE we have used the NDVI Thresholds Method proposed by *Sobrino and Raissouni* [2000] and *Sobrino et al.* [2008]. This methodology uses certain NDVI thresholds to distinguish between soil pixels ($NDVI < NDVI_s$), pixels of full vegetation ($NDVI > NDVI_v$) and pixels composed of soil and vegetation (mixed pixels, $NDVI_s \leq NDVI \leq NDVI_v$) following this algorithm:

$$LSE = \begin{cases} a + b\rho_{red} & NDVI < NDVI_s \\ \varepsilon_v P_V + \varepsilon_s(1 - P_V) + C & NDVI_s \leq NDVI \leq NDVI_v \\ \varepsilon_v + C & NDVI > NDVI_v \end{cases}, \quad (15)$$

where ε_v and ε_s are respectively the soil and vegetation emissivities, PV is the proportion of vegetation, C is a term which takes into account the cavity effect due to surface roughness and a and b are spectra statistical fit coefficients.

[43] Values of ε_v and ε_s can be taken from the bibliography [*Rubio et al.*, 1997] or spectral libraries such as the ASTER spectral library (http://speclib.jpl.nasa.gov). In this case, the methodology estimates the surface emissivity of bare soil pixels ($NDVI < NDVI_s$ case) from reflectivity values (ρred) obtained with a sensor band located in the red region (in the case of Landsat 5 TM and Landsat 7 ETM+, band 3), in order to retrieve soil emissivity from image-based data. The relationship between emissivities and red reflectivities is assumed to be linear, and coefficients a and b are obtained from laboratory spectra of soils and statistical fits. However, in the case of Landsat this is not a critical question, since its thermal band is located in the region $10-12$ μm, where the emissivity correction is minimized. The analysis of the soil spectra included in the ASTER library shows a emissivity range between 0.96 and 0.98, so a value a fixed value of 0.97 could be chosen as a first approximation. When the pixel is considered as fully vegetated (PV = 1), $NDVI > NDVI_v$ case in equation (15), typical constant values of $\varepsilon v = 0.985$ and $C = 0.005$ are considered and, therefore, a value of 0.99 for fully vegetated pixels is finally set. It is important to note that equation (15) is only valid for a mixed area, so this expression does not reflect the cavity effects produced in a rough but homogeneous area.

[44] Using the geometrical model proposed by *Sobrino et al.* [1990], the cavity term (C) for a mixed area and near nadir view is given by

$$C = (1 - \varepsilon_s)\varepsilon_v F'(1 - P_V), \quad (16)$$

where F' is a geometrical factor ranging between 0 and 1 depending on the geometrical distribution of the surface. Since F' cannot be estimated from VNIR/TIR remote sensing data, a mean value is generally chosen [*Sobrino and Raissouni*, 2000].

[45] According to *Carlson and Ripley* [1997], PV is computed as follows:

$$P_V = \left(\frac{NDVI - NDVI_s}{NDVI_V - NDVI_s}\right)^2. \quad (17)$$

[46] Over particular areas, $NDVI_v$ and $NDVI_s$ values can be extracted from the NDVI histogram. Values of $NDVI_v = 0.5$ and $NDVI_s = 0.2$ were proposed by *Sobrino and Raissouni* [2000] to apply the method in global conditions. In order to obtain consistent values of PV, it must be set to zero for pixels with $NDVI < NDVI_s$ and set to one for pixels with $NDVI > NDVI_v$.

[47] Although we have no direct estimates of LSE, the LSE methodology used in this work gives an error of 1% between modeled and field measurements of LSE [*Sobrino et al.*, 2008].

[48] The computation of the atmospheric and meteorological variables has been carried out using the following methodologies.

3.2.5. Water Vapor

[49] There are two main sources of water vapor that are usually employed in LST retrieval models: local point data and remote sensing estimations. One of the most frequently used local point data is the atmospheric radiosounding from which water vapor is retrieved by means of a radiative transfer code such as MODTRAN 4.0, as mentioned in section 2.2. In the case of Landsat, there is also a web site from which a user can obtain water vapor and atmospheric radiances. This web site is based on MODTRAN computations and weather simulation [*Barsi et al.*, 2005] on a global scale. However, both of them are local point data and cannot be applied over an entire Landsat scene with heterogeneous and/or mountainous landscape.

[50] For large areas, remote sensing offers estimations of water vapor mainly developed using coarse resolution remote sensing data like NOAA AVHRR [*Sobrino et al.*, 2002], Terra/Aqua MODIS data [*Sobrino and El Kharraz*, 2003] and ERS-2 ATSR-2 [*Li et al.*, 2003], with an RMSE of about 0.5 g cm^{-2} making them useful in LST retrieval algorithms. In this work we have used Terra MODIS Level 2 water vapor product (Gao and Kaufman, online document, 1998) (MOD05_L2, and henceforth referred to as $MODIS_w$) because this satellite passes over our study area more or less at the same time as Landsat does, between 1000 and 1100 local solar time.

3.2.6. Air Temperature Modeling

[51] Air temperature data introduced in LST retrieval models are usually taken from meteorological ground stations at satellite overpass or, if available, from the first layer of atmospheric radiosoundings. However, in these studies there is no mention of how to spatially extend this variable to atmospherically correct all pixels in one or more Landsat scenes (180 by 185 km).

[52] To regionalize air temperature, we have applied a multiple regression analysis combined with spatial interpo-

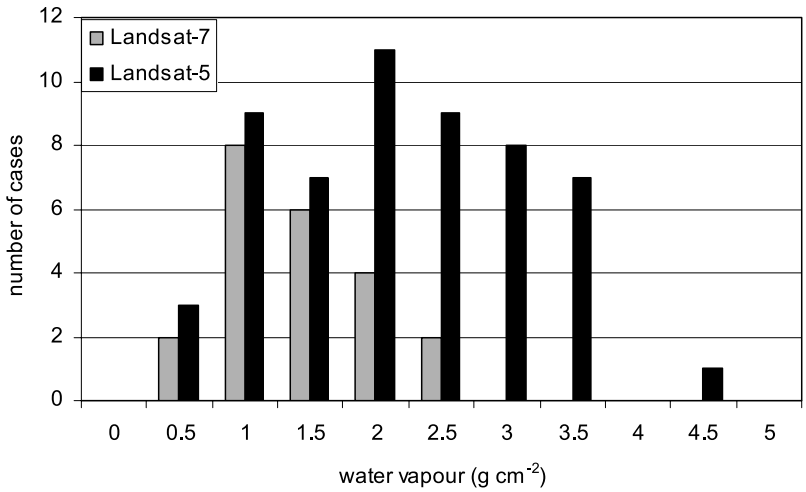

Figure 5. Histogram of the w obtained by the radiosoundings in the case of Landsat 5 and Landsat 7 images used to validate the LST models.

lation techniques [*Cristóbal et al.*, 2008; *Ninyerola et al.*, 2000, 2007]. Air temperature models (henceforth referred to as T_{am}) have been fitted using 60% of the meteorological ground stations and cross-validated with the remaining 40%. In these works, air temperature at the time of Landsat pass has been modeled obtaining a RMSE of 1.8 K (independent test) making it useful as an input variable to retrieve LST.

3.2.7. Atmospheric Parameters

[53] $L\downarrow$, $L\uparrow$ and τ have been obtained by a simulation procedure using MODTRAN 4.0 radiative transfer code as explained in section 2.2.

4. Model Test With Independent Data: Results

[54] In this section, we present the results obtained in the testing of the methods explained in section 2. Although the proposed methodology has also been developed by Landsat 4 TM, in the SCM atmospheric radiosoundings database there is only information after 1997 and, therefore, we cannot test Landsat 4 TM images. However, we expect Landsat 4 TM LST models to show similar results to the Landsat 5 TM and Landsat 7 ETM+ cases.

[55] In order to test the LST retrieval models and the variables it involves (emissivity, water vapor and air temperature) in situ measured values are needed. In our case, air temperature is the only variable that has been tested with a test set but, unfortunately, the rest of the data required to perform the test are not available at satellite pass. However, in the case of water vapor we have a set of atmospheric radiosoundings launched at 12:00 UTC from which we have computed $L\downarrow$, $L\uparrow$, τ and w using the MODTRAN 4.0 code. With these variables and emissivity, we have calculated LST using the RTE (equation (1)) from all test sites. This LST was established as the reference LST (LST_r) and used to compare the LST obtained by the models.

[56] Finally, in this section we also compare our proposed model with another existing LST retrieval operative methodology developed by *Qin et al.* [2001].

4.1. Air Temperature Test

[57] As mentioned in section 3.2, T_{am}s have been tested using 40% of the ground meteorological stations. We have obtained a mean RMSE of 1.8 and a σ of 0.4 K with a minimum value of 0.9 and a maximum value of 2.7 K. These values coincide with previous articles [*Cristóbal et al.*, 2008; Ninyerola et al. 2000, 2007].

4.2. Water Vapor Test

[58] The w obtained by the radiosoundings displays a mean of 1.59 and a σ of 0.84 g cm^{-2} with a minimum of 0.28 and a maximum of 3.73 g cm^{-2}. Figure 5 shows that Landsat 7 images are mainly located in the low w range (autumn and winter dates). On the other hand, Landsat 5 images are well balanced over the year covering different w situations.

[59] $MODIS_w$ displays a mean of 1.80 and a σ of 0.92 g cm^{-2} with a minimum of 0.30 and a maximum of 4.15 g cm^{-2}. The RMSE obtained with these two sources of water vapor, taking as reference the w of the radiosoundings, is 0.37 g cm^{-2} with a mean bias of 0.27 and a σ bias of 0.25. The results obtained coincide with the Terra MODIS water vapor error [*Sobrino and El Kharraz*, 2003] and demonstrate that remote sensing sources of water vapor are optimal for use as input variables in LST retrieval.

4.3. Land Surface Temperature Test

[60] The test of LST retrieval methodologies has been carried out using test sites (see Figure 4). As mentioned above, we have chosen the LST obtained by equation (1) as the reference LST.

[61] This test was performed using w and T_a from the radiosoundings and w and T_a from remote sensing and air temperature modeling ($MODIS_w$ and T_{am}, respectively) as input data for the LST models (see Figure 1). Table 7 shows the mean test results for all the test sites (see Figure 4 and Table 5) using w and T_a from the radiosoundings and $MODIS_w$ and T_{am}.

Table 7. Mean LST Validation Results Using Radiosoundings Data and $MODIS_w$ and T_{am} as Input Data for the LST Retrieval Developed Using TIGR-1, TIGR-2, TIGR-3, STD Atmospheric Databases, and *Qin et al.* [2001] Methodology[a]

		Radiosounding Data			$MODIS_w$ and T_{am}			
Atmospheric Database	Accuracy Estimator	LSTw	LSTwT	LSTT	LSTw	LSTwT	LSTT	n
TIGR-1	b	−1.18	0.35	−3.34	−1.44	0.22	−3.75	570
	σ_b	1.14	0.89	6.05	1.48	0.88	5.70	
	RMSE	1.64	0.96	6.91	2.07	0.90	6.82	
TIGR-2	b	−1.69	0.18	−2.62	−1.98	−0.02	−2.86	
	σ_b	1.51	0.90	5.03	1.92	0.96	4.79	
	RMSE	2.26	0.92	5.67	2.76	0.96	5.58	
TIGR-3	b	−1.01	−0.25	−3.78	−1.28	−0.33	−4.16	
	σ_b	1.15	0.96	7.60	1.58	1.02	7.26	
	RMSE	1.53	0.99	9.76	2.03	0.98	9.60	
STD	b	−1.50	0.91	−4.39	−1.81	0.76	−4.77	
	σ_b	1.37	1.75	5.86	1.83	1.71	5.60	
	RMSE	2.03	1.97	7.32	2.57	1.87	7.35	
LSTQin	b		−1.17			−1.27		363*/379
	σ_b		1.09			1.28		
	RMSE		1.64			1.56		

[a]LSTQin, *Qin et al.* [2001] methodology; w, water vapor; T, air temperature. RMSE (Kelvins), b (bias in Kelvins), and σ_b (bias standard deviation computed from the "n" number of samples, in Kelvins) have been computed using all test areas in Table 5 and Figure 4. The asterisk denotes the number of samples in the case of using radiosounding data.

[62] In the case of using w and T_a from the radio soundings, columns 3–5 of Table 7 show that, of all the atmospheric databases analyzed, the best LST retrieval models are those that include w and T_a (LSTwT). LSTwT models developed using TIGR-2, TIGR-1 and TIGR-3 display the best RMSE, 0.92, 0.96 and 0.99 K, respectively, followed by STD, 1.97. LSTw models developed using TIGR-3 and TIGR-1 also offer good RMSE, 1.53 and 1.64 K respectively, followed by STD and TIGR-2, 1.97 and 2.26 K, respectively. LSTT models display the worst results while TIGR-2 and TIGR-1 are better than STD and TIGR-3 (5.67, 6.91, 7.32, and 9.76 K, respectively) and the worst coefficients of determination, R^2 (see Table 4). This model is unable to retrieve LST with enough accuracy. Finally, in the case of *Qin et al.* [2001] methodology (LSTQin) the results show an RMSE of 1.64 K close to LSTwT models. It should be pointed out that LSTwT models show that the inclusion of T_a improves LST RMSE by more than 0.5 K compared with LSTw models and the LSTQin model.

[63] Results obtained using $MODIS_w$ and T_{am} as input data in LST retrieval (columns 6–8 of Table 7) display more or less the same pattern as the results obtained using w and T_a from radiosoundings, except in the case of LSTw models, in which the RMSE is higher. These results also suggest that LSTw models are more sensitive to an error in the source of w than LSTwT models, when it seems that the error is compensated by the inclusion of T_a in LST retrieval models. It is worth noting that LSTwT models show that the inclusion of T_a improves LST RMSE by more than 1 K compared with LSTw models. Furthermore, it should be noted that TIGR-1 offers lower RMSE results (0.90 K) than TIGR-2 (0.96 K) in the case of LSTwT models.

[64] In addition and in the case of LSTwT models, results obtained using w and T_a from radiosoundings and those obtained from $MODIS_w$ and T_{am} offer similar RMSE, approximately 0.9 K. These results are in agreement with one of the goals of this methodology that is the avoidance in the dependence on radiosounding data and show that the inclusion of $MODIS_w$ and T_{am} as input data is as useful as radiosounding data but being $MODIS_w$ and T_{am} the best option to retrieve LST over extensive areas.

[65] Table 7 also shows that LSTwT models offer the lowest bias (close to 0) for all TIGR atmospheric databases except STD. LSTw models show higher bias than LSTwT but lower than LSTT models, which display the worst results. In the case of LSTwT models, bias is always negative, which implies that these models tend to overestimate LST. On the other hand, LSTw and LSTT models tend to underestimate LST (except in the case of TIGR-3).

[66] To illustrate this fact, in Figure 6 we have selected models, using w and T_a from radiosoundings, that were developed using TIGR-1 and the LSTQin model. In Figure 7, we have used $MODIS_w$ and T_{am}, instead. We have excluded models developed using only T_a owing to the high RMSE obtained, which makes them inoperative. In both Figures 6 and 7 the behavior of the models is similar. In the w interval established between 0 to 2 g cm^{-2} the difference between LST_r and LSTwT remains mainly between −1 and 1 K (Figures 6 and 7). However, in LSTw and LSTQin models this difference increases over this interval by an increment of w (Figure 6). In the case of $MODIS_w$ and T_{am}, this increment is higher, going from −2 to 2 K (Figure 7). In the w interval region between 2 and 3 g cm^{-2} all models experience dispersion on the LST difference. However, the dispersion of the LSTwT model is lower, mainly between −1 and 2 K (Figures 6 and 7), than for the LSTw model, which is between −2 and −4 K. In the case of LSTQin models this dispersion is between 1 and 3.5 K. Beyond 3 g cm^{-2}, LSTwT mainly behaves in the same way as the 2–3 g cm^{-2} interval and LSTw increases steadily. It should be taken into account that LSTQin was only developed for a w interval from 0 to 3 g cm^{-2} and there is no comparison of this method beyond this point.

[67] Finally, Table 8 shows the RMSE obtained depending on the Landsat mission and on the source of data used as an input for the model. In all cases, the LSTwT models offer betters results than the LSTw models. When using radiosounding w and T_a as an input in LSTwT models (columns 3–5 of Table 8), best results with Landsat 5 models are obtained using TIGR-3, with an RMSE of approximately 1 K, and with Landsat 7, using TIGR-1, with an RMSE of about 0.4 K. When using $MODIS_w$ and T_{am} as an input in LSTwT models (columns 6–8 of Table 8), best results in

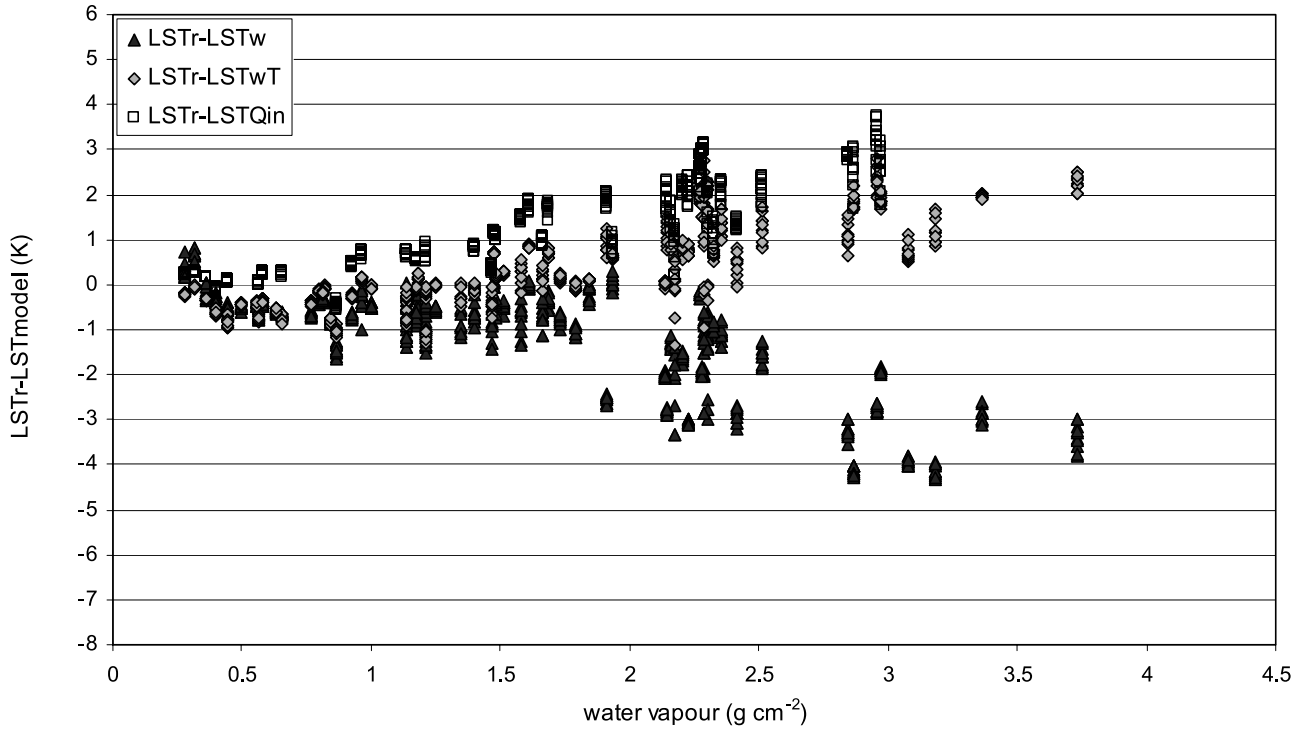

Figure 6. Differences between reference LST (LST_r) and modeled (in Kelvins) LST using TIGR-1 as atmospheric database and radiosounding *w* and T_a as input data. LSTw is the model developed using only *w*, LSTwT is the model developed using both *w* and T_a and LSTQin is the model developed by *Qin et al.* [2001].

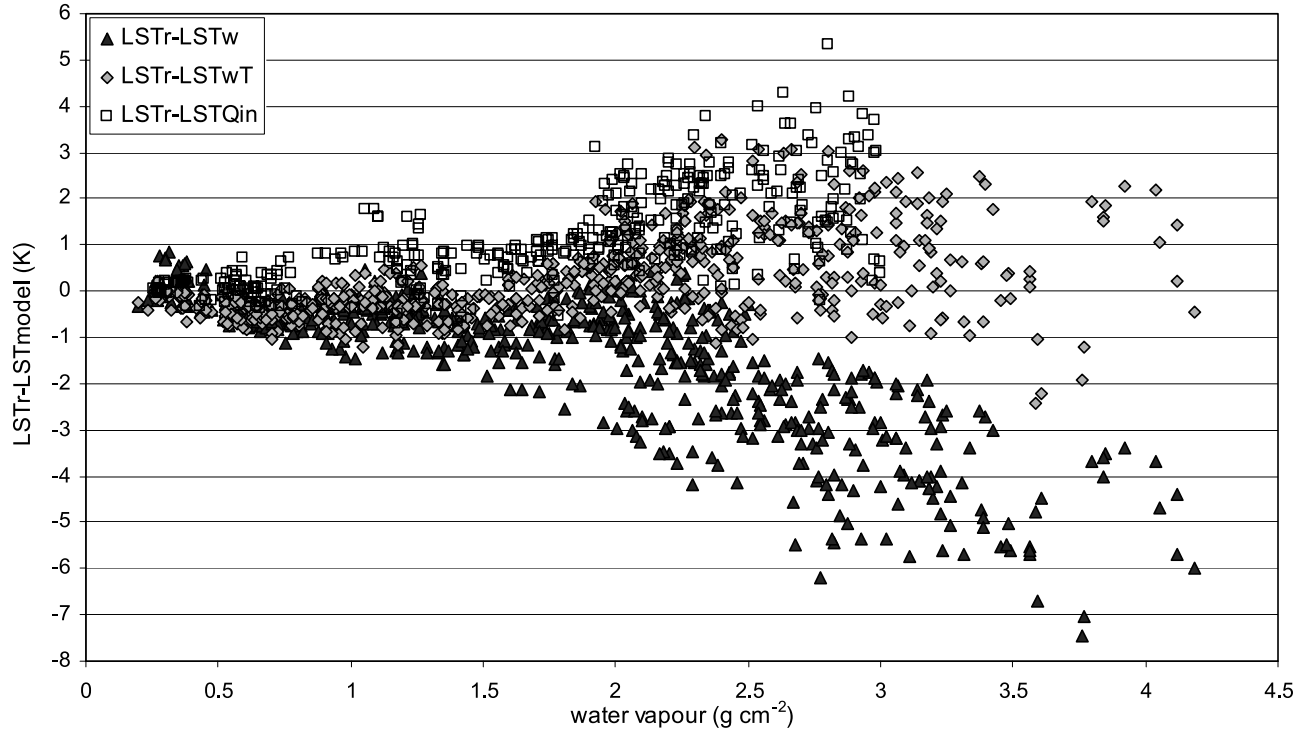

Figure 7. Differences between reference LST (LST_r) and modeled LST (in Kelvins) using TIGR-1 as atmospheric database and modeled *w* and T_a as input data. LSTw is the model developed using only *w*, LSTwT is the model developed using both *w* and T_a and LSTQin is the model developed by *Qin et al.* [2001].

Table 8. Mean RMSE Computed Using Radiosounding Data and $MODIS_w$ and T_{am} as LST Model Input for Each Landsat Mission[a]

		Radiosounding Data			$MODIS_w$ and T_{am}			
Atm. Base.	Satellite	LSTw	LSTwT	LSTT	LSTw	LSTwT	LSTT	n
TIGR-1	L5	1.87	1.11	7.91	2.35	1.03	7.83	399
	L7	0.88	0.39	3.56	1.17	0.51	3.41	171
TIGR-2	L5	2.61	1.04	6.53	3.15	1.04	6.44	399
	L7	1.10	0.51	2.75	1.47	0.73	2.58	171
TIGR-3	L5	1.76	1.02	9.76	2.33	1.12	9.66	399
	L7	0.72	0.91	4.10	1.03	0.95	3.86	171
STD	L5	2.33	2.32	8.42	2.93	2.19	8.47	399
	L7	1.02	0.61	3.54	1.37	0.66	3.51	171
Qin et al. [2001]	L5		1.64			1.56		363*/379

[a]Mean RMSE unit: Kelvins. Atm. Base is the model used to develop the LST retrieval method, L5 and L7 are Landsat 5 TM and Landsat 7 ETM+, respectively, w is water vapor, T is air temperature, and n is the number of samples. The asterisk denotes the number of samples in the case of using radiosounding data only in LSTQ in case.

Landsat 5 and Landsat 7 models have been obtained using TIGR-1 with an RMSE of 1.03 and 0.51, respectively. Note that in the case of Landsat 7, LSTwT and LSTw models provide closer results, with differences lower than 1 K. This fact can be explained because of the low atmospheric water vapor content for Landsat 7 scenes in comparison with Landsat 5 ones.

[68] In addition, except in the case of models developed using an STD atmospheric database, LSTwT models also offer better results than LSTQin, which is also developed using w and T_a. We should stress that the differences in RMSE between Landsat 5 and Landsat 7 are due to the number of images used (58 in Landsat 5 and 19 in Landsat 7) and the date. Most of the Landsat 7 images that were available from our study area were from autumn and winter, when w is low (see Figure 5) and, therefore, the correction is better as shown in Figures 6 and 7 (see range from 0 to 2 g cm^{-2}). With these results we cannot conclude that models developed for Landsat 7 are better than those developed for Landsat 5.

4.4. Atmospheric Database Selection

[69] The selection of the atmospheric database depends mainly on the range of w in the study area. As mentioned in section 3.2, our study area is located within a mean w value of 1.79 and a σ of 0.81 g cm^{-2} with a minimum of 0.16 and a maximum of 5.00 g cm^{-2}, if we take BCN as our reference point. The point located in Sort displays lower values of mean and σw. As mentioned in section 3.3.3, we obtained good results using all TIGR databases. However, it is worth noting that TIGR-1 offers the best results when using $MODIS_w$ and T_{am} as input data since it has a well-balanced w distribution. Moreover, this atmospheric database is a good option in the absence of radiosounding information to evaluate the w range (see Figure 2).

[70] In the case of the STD atmospheric database, and although it also has a well-balanced w range, results are worse than in the case of TIGR atmospheric databases and this fact suggests that this new radiosounding database has not worked properly in our study area.

5. Conclusions

[71] To sum up, the results show that the inclusion of T_a together with w in the single-channel LST models improves LST retrieval. The best RMSE, 0.9 K, was obtained using the TIGR-1 database, and shows lower error dispersion in intermediate and high atmospheric water vapor content. However, if T_a is not available, LST retrieval using only w is a good choice when the atmospheric water vapor content is low or intermediate. On the other hand, models that only include T_a have proven to be unable to retrieve LST and display the worst RMSE.

[72] When using w and T_a data from the radiosoundings, LSTwT models displayed an RMSE which is less than 0.5 K compared with LSTw. Moreover, when using $MODIS_w$ and T_{am} as input data, the improvement is greater than 1 K compared with LSTw models. This means that LSTw models are more sensitive to w obtained by remote sensing models than LSTwT in which the inclusion of T_a in the model helps to reduce the error. It is worth pointing out that LSTw and LSTT models tend to underestimate LST while LSTwT models tend to overestimate it. Moreover, in the case of LSTwT models, results obtained from radiosounding data and modeled data ($MODIS_w$ and T_{am}) offer similar results, being this fact in agreement with the aims of the presented LST retrieval methodology that is the avoidance in the dependence on radiosounding data to retrieve LST over extensive areas.

[73] In the case of the comparison between algorithms developed using both w and T_a, LSTwT also displays an RMSE that is less than 0.5 K compared with LSTQin. Moreover, it should be taken into account that LSTwT models are developed for w ranges that cover more than 3 g cm^{-2}.

[74] The best Landsat 5 TM and Landsat 7 ETM+ LST results have been obtained using TIGR-1 atmospheric databases and their RMSE are 1.03 and 0.51, respectively. However, a comparison between both satellites in LST retrieval models is not possible because of the different w range of the Landsat 5 and Landsat 7 series studied. In addition, it has been observed lower differences between LSTwT and LSTw models for the Landsat 7 scenes than the ones obtained for the Landsat 5 scenes, these last acquired with higher atmospheric water vapor content. This fact indicates, as is expected, that the improvement of the LSTwT models is more apparent for high water vapor contents (typically $w > 3$ g cm^{-2}).

[75] All TIGR databases have proven to be a powerful input data to develop models on a world-wide scale and for a wide range of w. Moreover, the best LST retrieval results have been obtained using TIGR-1, which is the most well-balanced w database, and in the case of nonavailability of

atmospheric water vapor information for a study area, using this database is the best option.

[76] Finally, at-satellite T_a models and the Terra MODIS w product have proven to be a good option for inclusion in a LST model to retrieve LST for large areas. This fact suggests that the use of radiosoundings as input data in LST retrieval models is not of primary importance, being T_a models and remote sensing estimations of w useful approximations to atmospherically correct Landsat series thermal band within a reasonable performance limit.

[77] **Acknowledgments.** The authors would like to thank B. Sebag and C. Crevoisier from the Laboratoire de Météorologie Dynamique/Groupe Analyse du Rayonnement Atmosphérique of the Ecole Polytechnique (Paris, France) for providing us with the TIGR-3 database and for their help in the database conversion to MODTRAN format. We would also like to thank our colleagues of the Department of Geography and CREAF of the UAB who have collaborated in any way in the treatment of the images, and INTA for its efficient image subscription service. It would not have been possible to carry out this study without the financial assistance of the Ministry of Science and Technology and the FEDER funds through the research project "Compression and interactive transmission of high-resolution images. Remote Sensing and Geographical Information Systems applications" (TSI2006-14005-C02-02). We would like to express our gratitude to the Catalan Water Agency and to the Ministry of the Environment and Housing of the Generalitat (Autonomous Government of Catalonia) for their investment policy and the availability of remote sensing data, which has made it possible to conduct this study under optimal conditions.

References

Achard, V. (1991), Trois problèmes clés de l'analyse tridimensionelle de la structure thermodynamique de l'atmosphère par satellite: Measure du contenu en ozone, classification des masses d'air, modélisation hyperrapide du transfert radiatif, Ph.D. dissertation, 168 pp., Univ. Pierre et Marie Curie, Paris.

Aires, F., A. Chédin, N. A. Scott, and W. B. Rossow (2002), A regularized neural net approach for retrieval of atmospheric and surface temperatures with the IASI instrument, *J. Appl. Meteorol.*, *41*, 144–159.

Allen, R. G., M. Tasumi, and R. Trezza (2007), Satellite-based energy balance for Mapping Evapotranspiration with Internalized Calibration (METRIC)-Model, *J. Irrig. Drain. Eng.*, *133*(4), 380–394.

Anderson, M., and W. Kustas (2008), Thermal remote sensing of drought and evapotranspiration, *Eos Trans. AGU*, *89*(26), 233, doi:10.1029/2008EO260001.

Barsi, J. A., J. R. Schott, F. D. Palluconi, D. L. Helder, S. J. Hook, B. L. Markham G. Chander, and E. M. O'Donnell (2003), Landsat TM and ETM+ thermal band calibration, *Can. J. Remote Sens.*, *29*, 141–153.

Barsi, J. A., J. R. Schott, F. D. Palluconi, and A. J. Hook (2005), Validation of a web-based atmospheric correction tool for single thermal band instruments, *Proc. SPIE*, *5882*, 136–142, doi:10.1117/12.619990.

Barsi, J. A., S. J. Hook, J. R. Schott, N. G. Raqueno, and B. L. Markham (2007), Landsat 5 Thematic Mapper thermal band calibration update, *IEEE Trans. Geosci. Remote Sens. Lett.*, *4*, 552–555.

Bartolucci, L. A., and M. Chang (1988), Look-up tables to convert Landsat TM thermal IR data to water surface temperatures, *Geocarto Int.*, *3*, 61–67.

Bastiaanssen, W. G. M., M. Meneti, R. A. Feddes, and A. A. M. Holtslag (1998), A remote sensing surface energy balance algorithm for land (SEBAL). 1. Formulation, *J. Hydrol.*, *212–213*, 198–212.

Carlson, T. N., and D. A. Ripley (1997), On the relation between NDVI, fractional vegetation cover, and leaf area index, *Remote Sens. Environ.*, *62*(3), 241–252.

Chédin, A., N. A. Scott, C. Wahiche, and P. Moulinier (1985), The improved initialization inversion method: A high resolution physical method for temperature retrievals from TIROS N series, *J. Clim. Appl. Meteorol.*, *24*, 128–143.

Chevallier, F., F. Chéruy, N. A. Scott, and A. Chédin (1998), Neural network approach for a fast and accurate computation of the longwave radiation budget, *J. Appl. Meteorol.*, *37*, 1385–1397.

Cristóbal, J., X. Pons, and P. Serra (2004), Sobre el uso operativo de Landsat 7 ETM+ en Europa, *Rev. Teledeteccion*, *21*, 55–59.

Cristóbal, J., X. Pons, and M. Ninyerola (2005), Modelling actual evapotranspiration in Catalonia (Spain) by means of remote sensing and geographical information systems, *Gottinger Geogr. Abh.*, *113*, 144–150.

Cristóbal, J., M. Ninyerola, and X. Pons (2008), Modeling air temperature through a combination of remote sensing and GIS data, *J. Geophys. Res.*, *113*, D13106, doi:10.1029/2007JD009318.

Dash, P., F. M. Göttsche, F. S. Olesen, and H. Fischer (2002), Land surface temperature and emissivity estimation from passive sensor data: Theory and practice-current trends, *Int. J. Remote Sens.*, *23*, 2563–2594.

Gibbons, D. E., G. E. Wukelik, J. P. Leighton, and M. J. Doyle (1989), Application of Landsat Thematic Mapper data for coastal thermal plume analysis at Diablo Canyon, *Photogramm. Eng. Remote Sens.*, *55*, 903–909.

Goetz, S. J., R. N. Halthore, F. G. Hall, and B. L. Markham (1995), Surface temperature retrieval in temperature grassland with multiresolution sensors, *J. Geophys. Res.*, *100*(D10), 25,397–25,410.

Hurtado, E., and J. A. Sobrino (2001), Daily net radiation estimated from air temperature and NOAA-AVHRR data: a case study for the Iberian Peninsula, *Int. J. Remote Sens.*, *8*, 1521–1533.

Hurtado, E., A. Vidal, and V. Caselles (1996), Comparison of two atmospheric correction methods for Landsat TM thermal band, *Int. J. Remote Sens.*, *17*, 237–247.

Irish, R. (2003), Landsat 7 Science Data Users Handbook, NASA Goddard Space Flight Cent., Greenbelt, Md. (Available at http://ltpwww.gsfc.nasa.gov/IAS/handbook/handbook_toc.html)

Jackson, R. D., R. J. Reginato, and S. B. Idso (1977), Wheat canopy temperature: A practical tool for evaluating water requirements, *Water. Resour. Res.*, *13*, 651–656.

Jackson, R. D., R. J. Reginato, S. B. Idso, and P. J. Pinter (1981), Canopy temperature as a crop water stress indicator, *Water. Resour. Res.*, *17*, 1133–1138.

Jiménez-Muñoz, J. C., and J. A. Sobrino (2003), A generalized single-channel method for retrieving land surface temperature from remote sensing data, *J. Geophys. Res.*, *108*(D22), 4688, doi:10.1029/2003JD003480.

Jiménez-Muñoz, J. C., and J. A. Sobrino (2006), Error sources on the land surface temperature retrieved from thermal infrared single channel remote sensing data, *Int. J. Remote Sens.*, *27*, 999–1014.

Jiménez-Muñoz, J. C., J. Cristóbal, J. A. Sobrino, G. Sória, M. Ninyerola, and X. Pons (2009), Revision of the single-channel algorithm for land surface temperature retrieval from Landsat thermal-infrared data, *IEEE Trans. Geosci. Remote Sens.*, *47*, 229–349, doi:10.1109/TGRS.2008.2007125.

Kaneko, T., and M. J. Wooster (1999), Landsat infrared analysis of fumarole activity at Unzen Volcano: Time-series comparison with gas and magma fluxes, *J. Volcanol. Geotherm. Res.*, *89*(1–4), 57–64.

Kneisys, F. X., et al. (1995), The MODTRAN 2/3 and LOWTRAN 7 model, report, Ontar Corp., North Andover, Mass.

Kustas, W. P. (1996), Use of remote sensing for evapotranspiration monitoring over land surfaces, *Hydrol. Sci. J.*, *41*, 495–516.

Kustas, W. P., A. N. French, J. L. Hatfield, T. J. Jackson, M. S. Moran, A. Rango, J. C. Ritchie, and T. J. Schmugge (2003), Remote sensing research in hydrometeorology, *Photogramm. Eng. Remote Sens.*, *69*, 631–646.

Kustas, W. P., J. M. Norman, T. J. Schmugge, and M. C. Anderson (2004), Mapping surface energy fluxes with radiometric temperature, in *Thermal Remote Sensing in Land Surface Processes*, edited by D. Quattrochi and J. Luvall, pp. 205–253, CRC Press, Boca Raton, Fla.

Li, Z.-L., L. Jia, Z.-B. Su, Z. Wan, and R. Zhang (2003), A new approach for retrieving precipitable water from ATSR2 split-window channel data over land area, *Int. J. Remote Sens.*, *24*, 5095–5117.

Mansor, S. B., and A. P. Cracknell (1994), Monitoring of underground coal fires using thermal infrared data, *Int. J. Remote Sens.*, *15*, 1675–1685.

Markham, B. L., and J. L. Barker (1986), Landsat MSS and TM post-calibration dynamic ranges, exoatmospheric reflectance and at-satellite temperatures, *EOSAT Landsat Tech. Notes 1*, pp. 3–8, Earth Obs. Satell. Co., Lanham, Md.

Moran, M. S., R. D. Jackson, L. H. Raymond, L. W. Gay, and P. N. Slater (1989), Mapping surface energy balance components by combining Landsat Thematic Mapper and ground-based meteorological data, *Remote Sens. Environ.*, *30*, 77–87.

Moran, M. S., T. R. Clarke, Y. Inoue, and A. Vidal (1994), Estimating crop water deficit using the relation between surface-air temperature and spectral vegetation index, *Remote Sens. Environ.*, *49*, 246–263.

Ninyerola, M., X. Pons, and J. M. Roure (2000), A methodological approach of climatological modelling of air temperature and precipitation through GIS techniques, *Int. J. Climatol.*, *20*, 1823–1841.

Ninyerola, M., X. Pons, and J. M. Roure (2007), Objective air temperature mapping for the Iberian Peninsula using spatial interpolation and GIS, *Int. J. Climatol.*, *27*, 1231–1242, doi:10.1002/joc.1462.

Palà, V., and X. Pons (1995), Incorporation of relief into geometric corrections based on polynomials, *Photogramm. Eng. Remote Sens.*, *61*, 935–944.

Pons, X., and L. Solé-Sugrañes (1994), A simple radiometric correction model to improve automatic mapping of vegetation from multispectral satellite data, *Remote Sens. Environ.*, *47*, 1–14.

Qin, Z., A. Karnieli, and P. Berliner (2001), A mono-window algorithm for retrieving land surface temperature from Landsat TM data and its

application to the Israel-Egypt border region, *Int. J. Remote Sens.*, *22*, 3719–3746.

Quattrochi, D. A., and J. C. Luvall (Eds.) (2000), *Thermal Remote Sensing in Land Surface Processes*, CRC Press, Boca Raton, Fla.

Riddering, J. P., and L. P. Queen (2006), Estimating near-surface air temperature with NOAA AVHRR, *Can. J. Remote. Sens.*, *32*, 33–43.

Rubio, E., V. Caselles, and C. Badenas (1997), Emissivity measurements of several soils and vegetation types in the 8–14 μm wave band: Analysis of two field methods, *Remote Sens. Environ.*, *59*, 490–521.

Saraf, A. K., A. Prakash, S. Sengupta, and R. P. Gupta (1995), Landsat TM data for estimating ground temperature and depth of subsurface coal fire in the Jharia coalfield, India, *Int. J. Remote Sens.*, *16*, 2111–2124.

Schneider, K., and W. Mauser (1996), Processing and accuracy of Landsat Thematic Mapper data for lake surface temperature measurement, *Int. J. Remote Sens.*, *17*, 2027–2041.

Schott, J. R., and W. J. Volchok (1985), Thematic Mapper thermal infrared calibration, *Photogramm. Eng. Remote Sens.*, *51*, 1351–1357.

Schott, J. R., J. A. Barsi, L. B. Nordgren, N. G. Raqueño, and D. De Alwis (2001), Calibration of Landsat thermal data and application to water resource studies, *Remote Sens. Environ.*, *78*, 108–117.

Scott, N. A., and A. Chedin (1981), A fast line by line method for atmospheric absorption computations: The automatized atmospheric absorption atlas, *J. Meteorol.*, *20*, 802–812.

Shanmugam, A. Y., J. Lee, and Y. Q. Kang (2006), Application of satellite infrared data for mapping of thermal plume contamination in coastal ecosystem of Korea, *Mar. Environ. Res.*, *61*(2), 186–201.

Sobrino, J. A., and J. El Kharraz (2003), Surface temperature and water vapor retrieval from MODIS data, *Int. J. Remote Sens.*, *24*, 5161–5182.

Sobrino, J. A., and N. Raissouni (2000), Toward remote sensing methods for land cover dynamic monitoring: Application to Morocco, *Int. J. Remote Sens.*, *21*, 353–366.

Sobrino, J. A., V. Caselles, and B. Becker (1990), Significance of the remotely sensed thermal infrared measurements obtained over a citrus orchard, *ISPRS J. Photogramm. Remote Sens.*, *44*, 345–354.

Sobrino, J. A., Z.-L. Li, and M. P. Stoll (1993), Impact of the atmospheric transmittance and total water vapor content in the algorithms for estimating satellite sea surface temperatures, *IEEE Trans. Geosci. Remote Sens.*, *31*, 946–952.

Sobrino, J. A., J. C. Jiménez-Muñoz, N. Raissouni, and G. Soria (2002), A simplified method for estimating the total water vapor content over sea surfaces using NOAA-AVHRR channels 4 and 5, *IEEE Trans. Geosci. Remote Sens.*, *40*, 357–361.

Sobrino, J. A., J. C. Jiménez-Muñoz, G. Sòria, M. Romaguera, L. Guanter, J. Moreno, A. Plaza, and P. Martínez (2008), Land surface emissivity retrieval from different VNIR and TIR sensors, *IEEE Trans. Geosci. Remote Sens.*, *46*, 316–327, doi:10.1109/TGRS.2007.904834.

Stathopoulou, M., and C. Cartalis (2007), Daytime urban heat islands from Landsat ETM+ and Corine land cover data: An application to major cities in Greece, *Sol. Energy*, *81*(3), 358–368.

Valor, E., and V. Caselles (2005), Validation of the vegetation cover method for land surface emissivity estimation, in *Recent Research Developments in Thermal Remote Sensing*, edited by V. Caselles, E. Valor, and C. Coll, pp. 1–20, Res. Signpost, Kerala, India.

Xian, G., and M. Crane (2006), An analysis of urban thermal characteristics and associated land cover in Tampa Bay and Las Vegas using Landsat satellite data, *Remote Sens. Environ.*, *104*, 147–156.

Yang, W., and L. Di (2004), An accurate and automated approach to georectification of HDF-EOS swath data, *Photogram. Eng. Remote Sens.*, *70*, 397–404.

Yang, X., Q. Zhou, and M. Melville (1997), Estimating local sugarcane evapotranspiration using Landsat TM image and VITT concept, *Int. J. Remote Sens.*, *18*, 453–459.

Zhang, X., and J. L. van Genderen (1997), A method to evaluate the capability of Landsat 5 TM band 6 data for sub-pixel coal fire detection, *Int. J. Remote Sens.*, *18*, 3279–3288.

J. Cristóbal and X. Pons, Department of Geography, Autonomous University of Barcelona, B-Building, E-08193 Cerdanyola del Vallès, Spain. (jordi.cristobal@uab.cat)

J. C. Jiménez-Muñoz and J. A. Sobrino, Global Change Unit, Imaging Processing Laboratory (IPL). Department of Earth Physics and Thermodynamics, University of Valencia, Poligono La Coma s/n., E-46980 Paterna, Spain.

M. Ninyerola, Unit of Botany, Department of Animal Biology, Plant Biology and Ecology, Autonomous University of Barcelona, C-Building, E-08193 Cerdanyola del Vallès, Spain.